Available online at www.sciencedirect.com
ScienceDirect
International Journal of Multiphase Flow 33 (2007) 317–332
International Journal of Multiphase Flow
www.elsevier.com/locate/ijmulflow

Three-dimensional numerical analysis of the deformation behavior of droplets impinging onto a solid substrate

Hitoshi Fujimoto [a,*], Yu Shiotani [b,1], Albert Y. Tong [c], Takayuki Hama [a], Hirohiko Takuda [a]

[a] *Department of Energy Science and Technology, Graduate School of Energy Science, Kyoto University, Yoshida-Honmachi, Sakyo-ku, Kyoto 606-8501, Japan*
[b] *Kyoto University, Kyoto 606-8501, Japan*
[c] *Department of Mechanical and Aerospace Engineering, University of Texas at Arlington, TX 76019-0023, USA*

Abstract

The collision dynamics of water droplets impacting onto a solid is studied by means of three-dimensional computer simulations. The Navier–Stokes equations for unsteady, incompressible, viscous fluids in the three-dimensional Cartesian coordinate system are approximated and solved by a finite difference method. The volume-of-fluid (VOF) technique is used to track the free liquid surface. Normal and oblique collisions of droplets with the substrate are simulated at low droplet impact inertia. The effect of impact angle on the deformation behavior of droplets is investigated. The experimental observations and the numerical results are in reasonable agreement. Theoretical aspects of the physics of the collision phenomena are addressed.

Keywords: Oblique collision; Droplet; Photographic; Three-dimensional numerical simulation

1. Introduction

Spray cooling is widely used in various industrial applications because of simplicity of hardware requirements and high heat transfer efficiency. Droplet impingement onto a solid surface occurs frequently in the process. As fundamental research on spray cooling, numerical studies on the collision of liquid droplets with a solid surface have been performed by the present authors (Hatta et al., 1995; Fujimoto and Hatta, 1996; Fujimoto et al., 2001; Fujimoto et al., 2004; Tong et al., 2004). Due to lack of computational resources and modeling challenges posed in three-dimensional simulations, these studies were carried out assuming that the collision of droplets with a solid be axisymmetric. Although they provided interesting information from

* Corresponding author. Tel.: +81 75 753 5419; fax: +81 75 753 5428.
E-mail address: h-fujimoto@energy.kyoto-u.ac.jp (H. Fujimoto).
[1] Present address: Matsushita Electric Co., Japan.

0301-9322/$ - see front matter © 2006 Elsevier Ltd. All rights reserved.
doi:10.1016/j.ijmultiphaseflow.2006.06.013

the aspects of fluid mechanics, two-dimensional analysis is applicable to only special cases and the physics of phenomena is usually three-dimensional.

There have been a few recent studies on the three-dimensional analysis of the deformation behavior of droplets impacting onto a solid substrate. A brief literature review is given here. Bussmann et al. (1999) developed a three-dimensional model based on the RIPPLE code (Kothe and Mjolsness, 1992) to model droplet impact. The effect of surface tension was taken into account by the continuum surface force (CSF) model (Brackbill et al., 1992). It was later applied to analyze the splash of a droplet impacting onto a solid (Bussmann et al., 2000). Pasandideh-Fard et al. (2002) extended Bussmann's model by including the effects of heat transfer and solidification of liquid drops. Ghafouri-Azar et al. (2003, 2004) investigated the interaction effect of molten metal droplets impinging onto a cold surface. Killion and Garimella (2004) performed a numerical simulation of the behavior of the falling film and pendant droplets in horizontal tube banks by the VOF technique (Hirt and Nichols, 1981). Wu et al. (2004) simulated the formation, ejection, and impact of a liquid droplet in an inkjet device by the VOF and CSF techniques. Ge and Fan (2005) carried out a three-dimensional simulation of a droplet impacting onto a hot flat surface in the Leidenfrost regime. The finite-volume method with the arbitrary Lagrangian–Eulerian technique was adopted.

Computational models for analyzing free surface flows have recently been reported in the literature. Droplet impact on a substrate has often been considered for the demonstration of the capabilities of the models. A brief review is given here. Baer et al. (2000) proposed a model for analyzing free surface flow by employing a finite element method (FEM). The motion of a droplet down an inclined plane was simulated. Perot and Nallapati (2003) utilized a moving unstructured staggered mesh method to study the collision of droplets onto a solid. Theodorakakos and Bergeles (2004) developed a model which combined the VOF method and the adaptive grid refinement method to simulate the impact of a small drop onto a solid. Tome et al. (2004) presented a simulation of a spreading drop on a flat surface by a finite difference method. Marker particles were used to track free liquid surface.

In the above studies, emphasis is placed more on the algorithm implementation rather than on the physics of the collision phenomena. The collision dynamics of a droplet impacting onto a solid in a three-dimensional coordinate system has not been examined in detail and complete understanding of the collision phenomena is lacking. In addition, there are many factors affecting the collision behavior of droplets, such as impact inertia of droplet, impact angle, and physical properties of the liquid, the effects of which on the flow of droplets remain unclear. Further study is needed for better understanding of the three-dimensional phenomena.

The present study is on the three-dimensional computer analysis of a droplet impacting onto a solid surface. The objective is to study the flow structure inside the droplet in detail. The focus is on the oblique collision of water droplets with a solid surface. It is assumed that the flows obey the Navier–Stokes equations for unsteady incompressible viscous fluids. The effects of gravity, viscosity, surface tension at the free liquid surface between water and air, and wettability between water and solid are taken into account. The conservation equations are approximated and solved by a finite difference method and a three-dimensional Cartesian coordinate system is used. The free liquid surface is tracked by the VOF method. Computer simulations are performed at isothermal conditions with constant thermo-fluid properties. The numerical results have been compared with experimental data for validation. The effect of impact angle on the deformation behavior of droplets is examined. Theoretical aspects of the flow structure are also investigated.

2. Experiments

A schematic of the experimental apparatus used in the present study for the collision behavior of liquid droplets with a solid substrate is shown in Fig. 1. A brief description of the experimental procedure is given here, details can be found in the authors' prior study (Fujimoto et al., 2004). Distilled water at room temperature, used as the test liquid, is issued from a nozzle where a stream of droplets is generated. The droplets are isolated at one droplet per rotation passing through a slot hole on the rotating disk. The droplets then fall vertically downward and impinge onto the test piece. The pre-impact diameter of droplets, d_p, is approximately 0.55 mm. The impact velocity of droplets, v_0, is approximately 2.7 or 4.0 m/s. It is controlled by adjusting the pressure in the reservoir. The surface flatness of the test piece is less than 0.0006 mm (per manufacturer

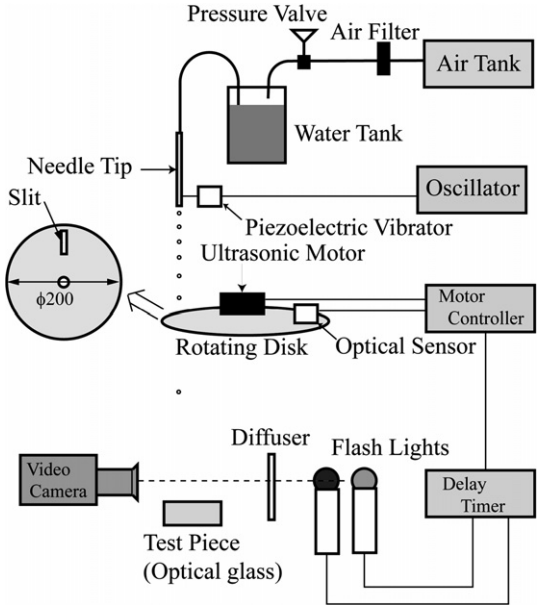

Fig. 1. A schematic of the experimental apparatus.

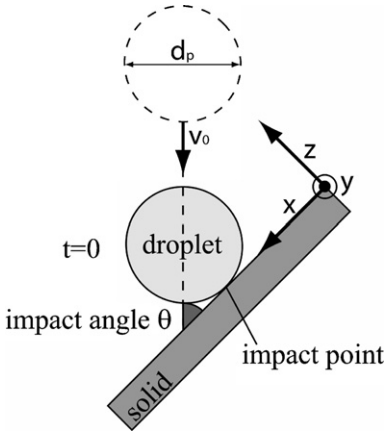

Fig. 2. A schematic of the collision of a droplet with a solid and the coordinate system.

specification). The impact angle, θ, as defined in Fig. 2, is set to 90°, 60°, 45°, and 30°. Note that the 90° case corresponds to normal collision.

A digital video camera along with two micro flashes is used for photographic observations. An optical sensor set at the rotating disk captures the motion of the slit hole and a signal is sent to a delay timer. When a droplet approaches a solid surface, a micro flash is activated by a trigger signal from the delay timer. A second micro flash is triggered afterward at a certain preset time delay, enabling double-exposure photographs taken for each droplet impact. Flash settings are set at various timings under a fixed experimental condition. The time duration of the flash is 2 μs. Photographs are arranged in chronological sequence to display the deformation process of droplets.

The spatial resolutions of droplet during the collision are obtained directly from the photographic images. The spatial measurement resolution is dependent on the magnification of the lens system. For oblique collisions, a droplet spreads further along an inclined solid surface than in normal collisions. In order to include the entire elongated droplets into a camera frame, magnification has to be set smaller than that for

normal collisions. The spatial resolution is within 0.04 mm and 0.02 mm for the oblique and normal collisions, respectively.

3. Numerical simulations

3.1. Conservation equations

A schematic of a droplet impact onto a substrate is shown in Fig. 2. A spherical water droplet with uniform velocity falls vertically in air, impinges onto a smooth horizontal or inclined solid substrate at room temperature. The time, t, is measured from the instant when the drop first touches the solid surface. The densities of air and water are set to 1.2 kg/m^3 and 1000 kg/m^3, respectively. The fluid density changes sharply at the free surface between water and air. The flows are assumed to obey the Navier–Stokes equations for incompressible viscous fluids in a three-dimensional Cartesian coordinate system maintained at isothermal condition with constant thermo-fluid properties. In the present model, the effects of gravity, viscosity, surface tension at free surface, and wettability between liquid and solid are taken into account. The conservation equations, consist of the continuity and momentum equations, are given by

$$\text{div } \mathbf{u} = 0 \tag{1}$$

and

$$\rho \frac{\mathrm{D}\mathbf{u}}{\mathrm{D}t} = -\text{grad } p + \mu \nabla^2 \mathbf{u} + \rho \mathbf{F} \tag{2}$$

where t, $\mathbf{u}(=(u, v, w))$ and p are time, velocity, and pressure. ρ, μ and $\mathbf{F}$ denote apparent fluid density, apparent viscosity and volume force, respectively.

The VOF technique is applied to track the time evolution of the free liquid surface. A color function, ϕ, is introduced to represent the volume fraction of liquid in a computational cell. If the control volume is filled with liquid alone, the color function is unity. When only air exists in the control volume, ϕ takes on a value of zero. When both liquid and air are present, the color function value lies between 0 and 1. The equation for the advection of the color function is given by

$$\frac{\mathrm{D}\phi}{\mathrm{D}t} = 0 \tag{3}$$

The apparent density and viscosity are given by

$$\rho = \rho_{\text{water}}\phi + \rho_{\text{air}}(1 - \phi) \tag{4}$$

$$\mu = \mu_{\text{water}}\phi + \mu_{\text{air}}(1 - \phi) \tag{5}$$

The volume force, $\mathbf{F}$, appearing in Eq. (2), consists of the gravitational force and the surface tension force (by means of the CSF model) is given by

$$\mathbf{F} = \rho g \mathbf{i} + \delta \sigma \kappa_s \nabla \phi \tag{6}$$

where g, δ, σ, κ_s, $\mathbf{i}$ represent gravitational acceleration, delta function at free surface, surface tension coefficient, local curvature of free surface, and unit vector in the direction of gravity, respectively. κ_s is given by

$$\kappa_s = -(\nabla \cdot \mathbf{n}) \tag{7}$$

where $\mathbf{n}$ is the unit normal to the free surface given by $\nabla\phi/|\nabla\phi|$.

3.2. Numerical procedure

The conservation equations are discretized and solved by a finite difference method. The computational domain is divided into numerous small cells. A staggered mesh is used where pressure, p, and density, ρ, are evaluated at the center and velocity components, u, v and w, are given at the edges of cells. The fractional step method (CCUP (CIP-combined and unified procedure)) developed by Yabe et al. (2001) is used to solve

the conservation equations. The momentum equations are approximated and decomposed into three parts utilizing a forward Euler scheme in the unsteady term

$$\frac{\bar{\mathbf{u}}-\mathbf{u}^n}{\Delta t}+(\mathbf{u}^n\cdot\nabla)\mathbf{u}^n=0 \tag{8}$$

$$\frac{\tilde{\mathbf{u}}-\bar{\mathbf{u}}}{\Delta t}=\frac{\mu}{\rho}\nabla^2\tilde{\mathbf{u}}+\mathbf{F}^n \tag{9}$$

$$\frac{\mathbf{u}^{n+1}-\tilde{\mathbf{u}}}{\Delta t}=-\frac{1}{\rho}\mathrm{grad}\ p^{n+1} \tag{10}$$

where the superscripts n and $n+1$ represent two consecutive time stages. $\bar{\mathbf{u}}$ and $\tilde{\mathbf{u}}$ are intermediate velocities. Δt is the time increment. From Eqs. (1) and (10), the following equation for pressure can be derived:

$$\nabla\cdot\left(\frac{1}{\rho}\nabla p^{n+1}\right)=\frac{\nabla\cdot\tilde{\mathbf{u}}}{\Delta t} \tag{11}$$

Eq. (8) is first solved for $\bar{\mathbf{u}}$ by the R-CIP (rational-cubic interpolation program, Yabe et al., 2001) scheme. $\tilde{\mathbf{u}}$ is then obtained from Eq. (9), an approximated diffusion equation, by a second-order central difference scheme where a fully implicit scheme is adopted for time integration. Next, the pressure profile is obtained from Eq. (11). Finally, the velocity components are obtained by integrating Eq. (10). The equation for the advection of the color function, Eq. (3), is solved by the R-CIP scheme. SLIC (simple line interface construction) method is adopted to reconstruct the free liquid surface.

The time increment, Δt, is controlled by the CFL (Courant–Friendrichs–Lewy) condition for numerical stability given by

$$\Delta t=f_{\mathrm{CFL}}\frac{1}{\mathrm{Max}\left(\frac{|u_i|}{\Delta x_i}\right)} \tag{12}$$

in which the CFL number, f_{CFL}, is set to 0.2 in this study and Δx_i is the mesh size.

A non-uniform mesh system focusing on the region near the solid surface is used. The mesh in the z-direction is given by

$$\begin{aligned} &z_k/d_{\mathrm{p}}=\frac{\exp(k\Delta\zeta)-1}{\exp(n_z\Delta\zeta)-1},\quad k=0,1,2,3,\ldots\\ &\text{and}\\ &z_k=2z_{k-1}-z_{k-2}\quad \text{for } (z_k-z_{k-1})>0.05 \end{aligned} \tag{13}$$

in which $\Delta\zeta=0.012$ and $n_z=70$ or 80. The subscript k denotes the mesh number, where $k=0$ coincides with the solid surface ($z=0$). It should be noticed that $\exp(\Delta\zeta)$ is the ratio of two successive mesh sizes. The mesh size in the z-direction increases upward with minimum mesh size located adjacent to the solid surface, because of the presence of a thin velocity boundary layer along the surface where the velocity gradient is large. Uniform mesh sizes are applied in the x- and y-directions. The dimensionless mesh sizes in the x- and y-directions, normalized by the pre-impact diameter of droplets, are set to 1/80 or 1/100.

The effects of mesh size, time increment, and size of computational domain on the predictions have been investigated. It is understood that grid convergence is of great importance. The most common way to demonstrate grid convergence is to repeat a computation on a grid with more grid points, and compare the two results. On the other hand, large computer resources (memory and computational time) are required in performing three-dimensional computer simulations. The number of cells used in the present study is limited to approximately 5 million. Due to the computer capacity limitation, the grid convergence test cannot be carried through to the fullest extent. A grid refinement has been performed on a smaller domain for a shorter run time. This corresponds to case D in Table 1. The results appear to suggest that reasonable convergence has been achieved. In addition, experimental results are used for comparison and serve as a mean for verification.

In the present study, normal and oblique collisions of droplets with a substrate are investigated (see Fig. 3). In both cases, half computational domain is used by taking advantage of the symmetric deformation behavior

Table 1
Details of computational conditions for Figs. 4 and 5

Case	Dimensionless mesh sizes (Δx, Δy)	n_z associated with mesh size in z-direction	Number of girds ($x/y/z$ directions)	CFL number
A: regular mesh	1/80	70	242/122/102	0.2
B: fine mesh	1/100	80	272/137/112	0.2
C: small time increment	1/80	70	242/122/102	0.1
D: small domain, finer mesh	1/120	80	272/137/112	0.2

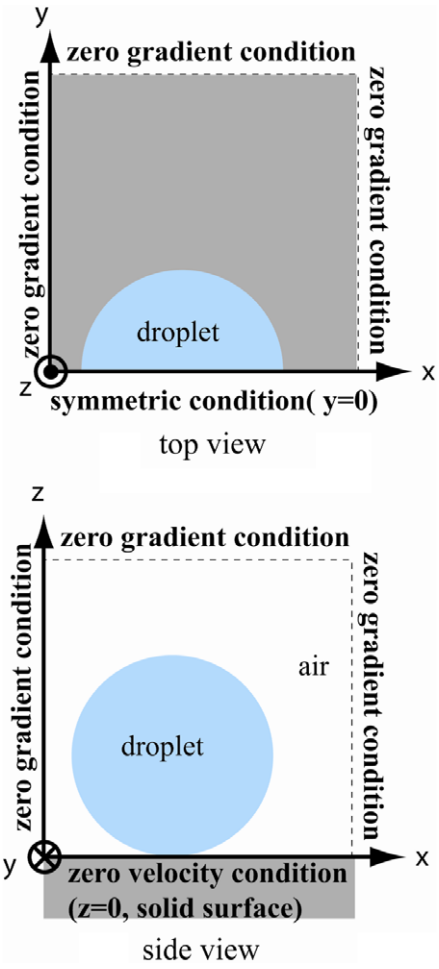

Fig. 3. Computational domains and boundary conditions.

of droplets imposed at $y = 0$. No-slip condition is employed along the wall boundary at $z = 0$ and zero gradient conditions are used at all other boundaries.

At the contact line, where free surfaces come into contact with a solid surface, a special treatment involving the contact angle is required. The contact angle is dependent on the wettability between liquid and solid and on the fluid motion relative to the wall (contact angle hysteresis). In the present study, a very simple method is applied to model the contact angle hysteresis. When the contact line advances along the dry surface, the advancing contact angle is specified to 110°. In receding, the contact angle is set to 35°. These values are obtained from experimental measurements.

In flow simulations involving a contact line, the basic approach for treating contact line motion is to consider the classical Young's equation. Such an approach has the practical difficulty of requiring the values of surface tension coefficients for all three inter-phases. Also it has been observed that employing the Young's equation will induce artificial flows near the contact line (Renardy et al., 2001). Another way of introducing a gradual change in the contact angle is to develop a mathematical relation between the contact angle and contact line velocity. Francois and Shyy (2003) formulated a dynamic contact angle model by linearly varying the contact angle values from advancing to receding, while the instantaneous contact line velocity transits from +5% to −5% of the initial impact velocity. The major drawback of such a formulation is that, by the time the droplet reaches its maximum spread, the contact angle value and the edge zone contour will already be modified to that of the recoiling mode and will begin receding immediately. Experimental observations have shown that the contact angle transition from advancing to receding values occurs at a constant spread diameter. This is the so-called contact angle hysteresis (E B Dussan, 1979), where the droplet stays at its maximum spread diameter while undergoing the transition from advancing to recoiling. The numerical formulation based on linearly varying the contact angle will negate such a process. The dynamic contact model implemented in the present study follows an approach of using just two contact angle values: one for advancing when the velocity is positive and another for receding when the velocity is negative. Basically, the linear variation is eliminated.

The contact angle is a very important parameter in the modeling of the liquid spread process. Unfortunately, very little is known about the details, either from a molecular or continuum point of view. The dynamic contact angle depends on the contact line velocity and in general will not remain constant during the entire spreading process. In the present study, the contact angles were measured experimentally in the following manner: a water drop is placed gently on a horizontal solid surface. Then, the solid surface is tilted gradually. The side view images of drops are taken before the drop begins to slide down along the solid. The advancing contact angle is determined by measuring the contact angle at lower edge, while the receding one is specified by the angle at upper edge. The same solid surface and liquid as in the impact test are used.

4. Results and discussion

4.1. Normal collision of a droplet with a solid substrate

The collision behavior of a single droplet impinging vertically onto a horizontal solid surface with $(d_p, v_0, \theta) = (0.56\ \text{mm}, 2.7\ \text{m/s}, 90°)$ is first studied. Since the impact angle is 90° and the impact inertia is relatively small, no splashing occurs and the deformation behavior of droplets is axis-symmetric. The internal flows of droplet are relatively simple compared to the fully three-dimensional flows in oblique collisions. The results for the normal impact of droplet are used for validation of the numerical model in the present study.

Fig. 4 depicts the comparison between experimental and numerical results for $(d_p, v_0, \theta) = (0.56\ \text{mm}, 2.7\ \text{m/s}, 90°)$. A dimensionless time, τ, is used where the physical time, t, is normalized by the pre-impact diameter and impact velocity of the droplet, as given in the figure. The values for the corresponding Reynolds (Re) and Weber (We) numbers, defined as

$$Re = \frac{\rho v_0 d_p}{\mu}, \quad We = \frac{\rho v_0^2 d_p}{\sigma} \tag{14}$$

are 1570 and 56, respectively. Numerical results obtained by using two meshes are used to investigate the effect of mesh size. The details of computational conditions are listed in Table 1. The droplet impinges onto the solid, deforms into the shape of a cap, and then becomes a thin circular disk. The two numerical results are very similar to each other although a slight difference is seen in later time stage as shown quantitatively in Fig. 5. In addition, the predictions are similar to the experiment for the entire process. In both experimental and numerical results, slight asymmetry of liquid shape is seen in the later time stage due to experimental difficulty for achieving axisymmetric flow motion and numerical errors caused by approximation method.

Fig. 5 represents the time evolution of the predicted and measured diameters of droplets on the horizontal solid surface for several computational conditions (see Table 1). The predicted and measured droplet heights from the solid surface are also compared for validation. The definitions of droplet diameter and height are

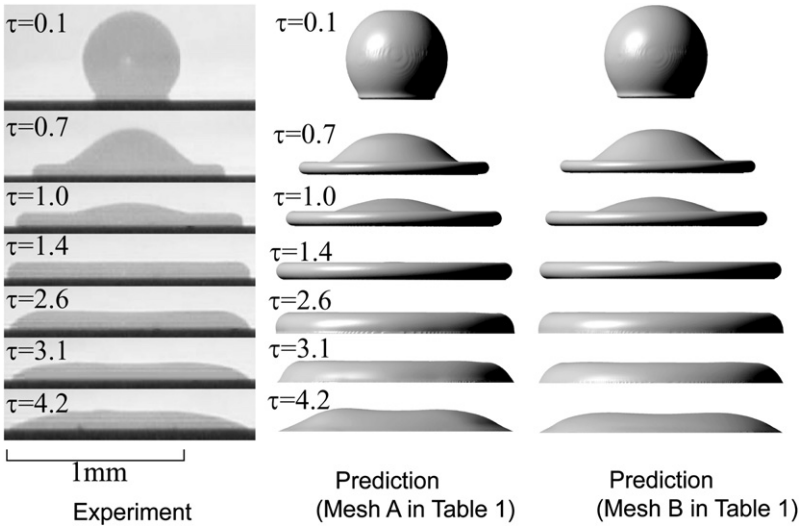

Fig. 4. Comparison of the deformation sequence between experiment and numerical prediction for $(d_p, v_0, \theta) = (0.56\ \text{mm}, 2.7\ \text{m/s}, 90°)$.

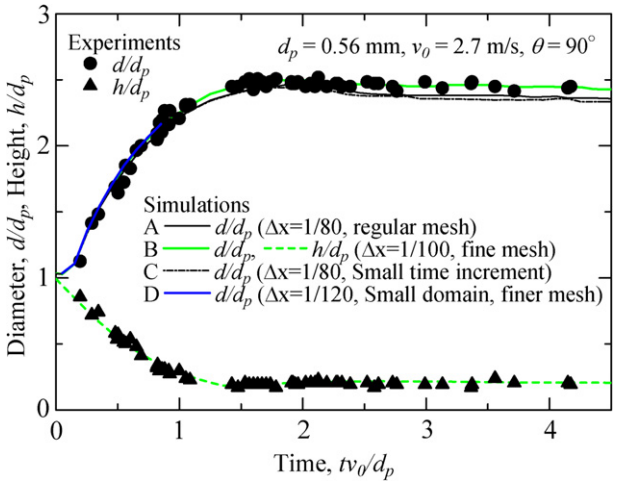

Fig. 5. Time evolution of droplet diameter and droplet height for $(d_p, v_0, \theta) = (0.56\ \text{mm}, 2.7\ \text{m/s}, 90°)$ with various computational conditions.

given in Fig. 6. As indicated in Figs. 4 and 5, the numerical results are in qualitative as well as quantitative agreement with the experiments. It is evident in Fig. 5 that the predictions are dependent on mesh sizes and time increment, although their effects are small. The predictions for case B (fine mesh) show the best fit to the experiments.

Fig. 7 shows the time evolution of the shape of droplet, the velocity profile and the pressure distribution inside the liquid of the droplet obtained with the use of the computational condition B in Table 1. It should be noticed that the liquid in the center region is thinner than that in the edge part. When the droplet is viewed laterally, as in Fig. 4, the sunken part cannot be seen because of the presence of a thick ring-shaped edge. p_r denotes atmospheric pressure in the figure.

A high-pressure region appears near the impact point shortly after the impact ($\tau = 0.1$). A thin circular liquid film is formed around the bottom edge of the droplet ($\tau = 0.7$). It spreads radially outward along the solid surface ($\tau = 1.0$–1.4) while the height of the droplet body decreases monotonically with time ($\tau = 0.7$–1.4). A velocity boundary layer develops along the solid surface. The radial velocity is zero at the center axis

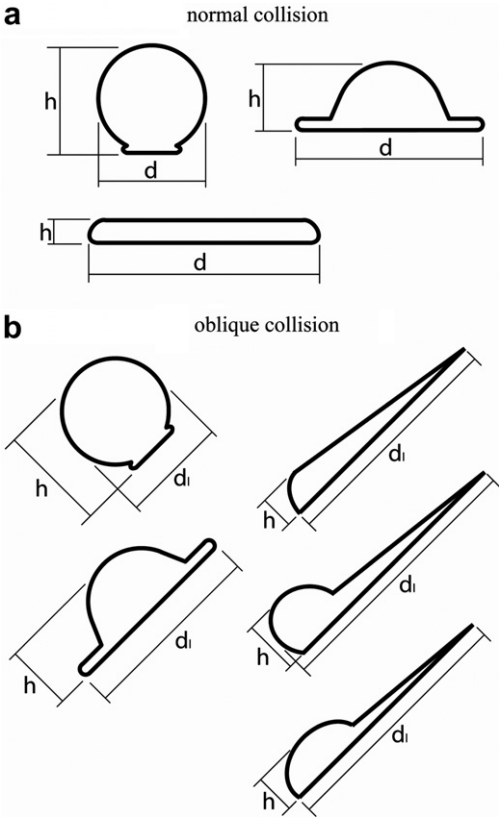

Fig. 6. Definition of droplet diameter and droplet height for normal collision (a) and spreading length and droplet height for oblique collision (b).

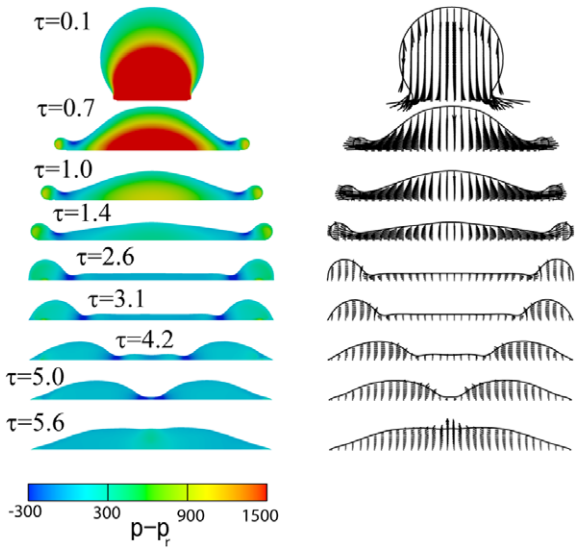

Fig. 7. Time evolution of the droplet shape, velocity profile and pressure distribution inside the liquid on a horizontal solid surface.

and increases radially. The droplet then deforms into a thin circular disk ($\tau = 2.6$). The leading edge of thin liquid film is round due to the effect of surface tension. The pressure in the leading edge is relatively high and

that in the concaved part adjacent to the leading edge is relatively low. The edge of the film is thicker than that near the impact point in the later time stages ($\tau = 2.6$–4.2). The liquid velocity decreases due to surface tension, wall friction, and internal viscous shear. Eventually, a recoiling flow from the edge to the center arises due to surface tension ($\tau = 3.1$–4.2). The flows eventually merge at the center and an upward flow arises ($\tau = 5.6$).

The motion of predicted contact angles is focused upon. In the spreading process, the contact angle is equal to the advancing angle. After the droplet reaches a maximum diameter, the contact angle decreases with time and then reaches the receding contact angle. It is found in Fig. 4 that the predicted contact angle is larger than the experiments at $\tau = 2.6$ and 3.1, while it is smaller at $\tau = 4.2$. It appears that the contact angle transition during the process from advancing to receding is not in full agreement with the experiments. The reasons for the discrepancy between predictions and experiments include: over-simplified modeling for contact angles, numerical errors, and experimental difficulties to ensure axisymmetric motion of droplets. Nevertheless, the predictions agree reasonably well with the experiments.

4.2. Oblique collision of a droplet with a solid substrate

The oblique collision of droplets with a solid substrate is examined where $(d_p, v_0, \theta) = (0.56\text{ mm}, 2.8\text{ m/s}, 45°)$. The corresponding Reynolds and Weber numbers are 1630 and 60, respectively. The pre-impact diameter and impact velocity of droplet are very similar to the case in the normal collision and the effect of impact angle on the collision behavior can be singled out by comparing the two results. Fig. 8 depicts the time evolution of the predicted and observed shapes of the droplet during the collision. The dimensionless mesh size is 1/100 in x- and y-directions and $n_z = 70$ in Eq. (13). The number of meshes is $402 \times 122 \times 102$ in x-, y-, and z-directions. It is obvious that the predictions agree qualitatively well with the experiments. The droplet impacts on the solid and a circular thin liquid film is formed around the bottom of the droplet. The liquid film spreads with time, while the height of the droplet decreases monotonically. The shape of liquid droplet becomes asymmetric. The lower edge of liquid is rounded and thick at $\tau = 4.5$ while other portion is very thin. Most of the liquid droplet is accumulated on the lower surface side. By comparing the results in Figs. 4 and 8, it is apparent that the spreading length of droplet along the inclined solid surface is larger than the spreading diameter of droplet for normal collision.

Quantitative comparison of numerical results with the experiments is shown in Fig. 9. The measured liquid length along the inclined surface increases monotonically with time. The measured height of droplet decreases with time, reaches a minimum, and then slightly increases. The calculated liquid length along the inclined surface is in good agreement with the experiments in the early time stages ($\tau = 0.0$–4.0), and slightly under predicted in the later time stages. Judging from the fact that the predicted contact line at the upper-edge remains stationary for $\tau > 0.4$ and it is consistent with the experiments, the predicted motion of the contact line at the lower-edge is slightly slower than the experiment. It should be noted that since numerical errors accumulate with time, the disagreement with experiments in the later time stage is perhaps not unexpected.

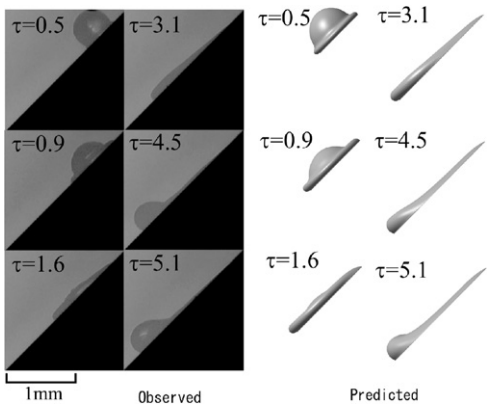

Fig. 8. Comparison of experiments with predictions for (0.56 mm, 2.8 m/s, 45°).

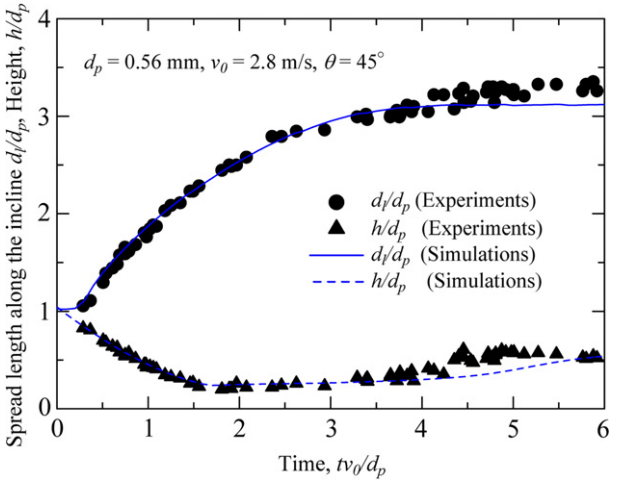

Fig. 9. Time evolution of spreading length of liquid along x-axis and liquid height for (d_p, v_0, θ) = (0.56 mm, 2.8 m/s, 45°).

The time evolutions of the droplet shape in bird's eye view are shown in Fig. 10a. The cross-section shape at $y = 0$ (x–z plane) along with velocity profile and pressure distribution in the liquid are displayed in Fig. 10b. The color mapping scale for pressure is the same at every time step. The magnitude of velocity vector is also the same except at $\tau = 6.0$. A high-pressure region appears near the impact point after the collision ($\tau = 0.2$ in Fig. 10b). A flow arises along the solid surface from the impact point, resulting in the formation of a thin liquid film around the bottom edge of droplet ($\tau = 0.2$, 0.5). The liquid film spreads radially along the solid surface. At $\tau = 0.5$, as shown in Fig. 10a, the droplet looks like a cap. The deformation behavior of the droplet is similar to that of the normal collision in early time stages. However, the flow inside the liquid is asymmetric as shown in Fig. 10b. The fluid moves downward due to the impact inertia of the droplet on an inclined plane. The velocity component in the x-direction is larger in the leading edge at the lower region. A slow upward flow appears in the upper edge region as well. A stagnation point appears near the upper edge. Since the no-slip condition is imposed at the solid boundary, a velocity boundary layer develops along the solid surface.

As shown in Fig. 10b, at $\tau = 0.9$, the liquid in the lower edge region is slightly thicker than that in the upper edge region. The liquid film spreads obliquely downward along the symmetric plane. The velocity is very small near the upper edge and is relatively larger in the lower part. It is noted that the predicted contact line at the upper-end remains stationary for $\tau > 0.4$. This trend is consistent with experiments. A weak vortex is seen near the upper edge.

At $\tau = 1.6$, in Fig. 10a, the droplet appears like a thin oval disk. As expected, the horizontal width of the oval thin liquid in the y-direction is smaller than the spreading length of droplet in the x-direction. Most of the fluid continues to move downwards, particularly near the lower edge. The upper and lower edges of the liquid are rounded due to surface tension and is convex lens-shaped at the center where the liquid pressure is higher than the surrounding air pressure. It should be noted that the sunken shape of the liquid cannot be reviewed by the side view images in Fig. 8.

At $\tau = 2.3$–5.1 in Fig. 10a, the liquid is accumulated in the circular edge. The thin oval liquid has a dimple at the center. The spreading length of the liquid in the y-direction reaches a maximum at $\tau \sim 2.3$ before reducing slightly afterward. After $\tau \sim 2.3$, the circular edge in the lower region not only flows along the surface (x-axis), but also moves to the symmetric plane ($y = 0$). As a consequence, most of the liquid is accumulated in the lower edge near the symmetric plane. Fig. 10c represents the velocity profile at $\tau = 4.5$. Flows from the edge to the symmetric plane are clearly shown. Coalescence of such flows at the symmetric plane causes an upward flow just downstream of the dimple. The liquid shrinks continuously in the y-direction. At $\tau = 5.1$ and 6.0, the liquid swelling at the bottom tip, due to the horizontal motion of the fluid, becomes very pronounced.

In Fig. 10b, the liquid elongates monotonically in the x-direction (the downward direction) until $\tau \sim 4.0$ (see also Fig. 9) when the velocity component in the x-direction at the symmetric plane decreases appreciably

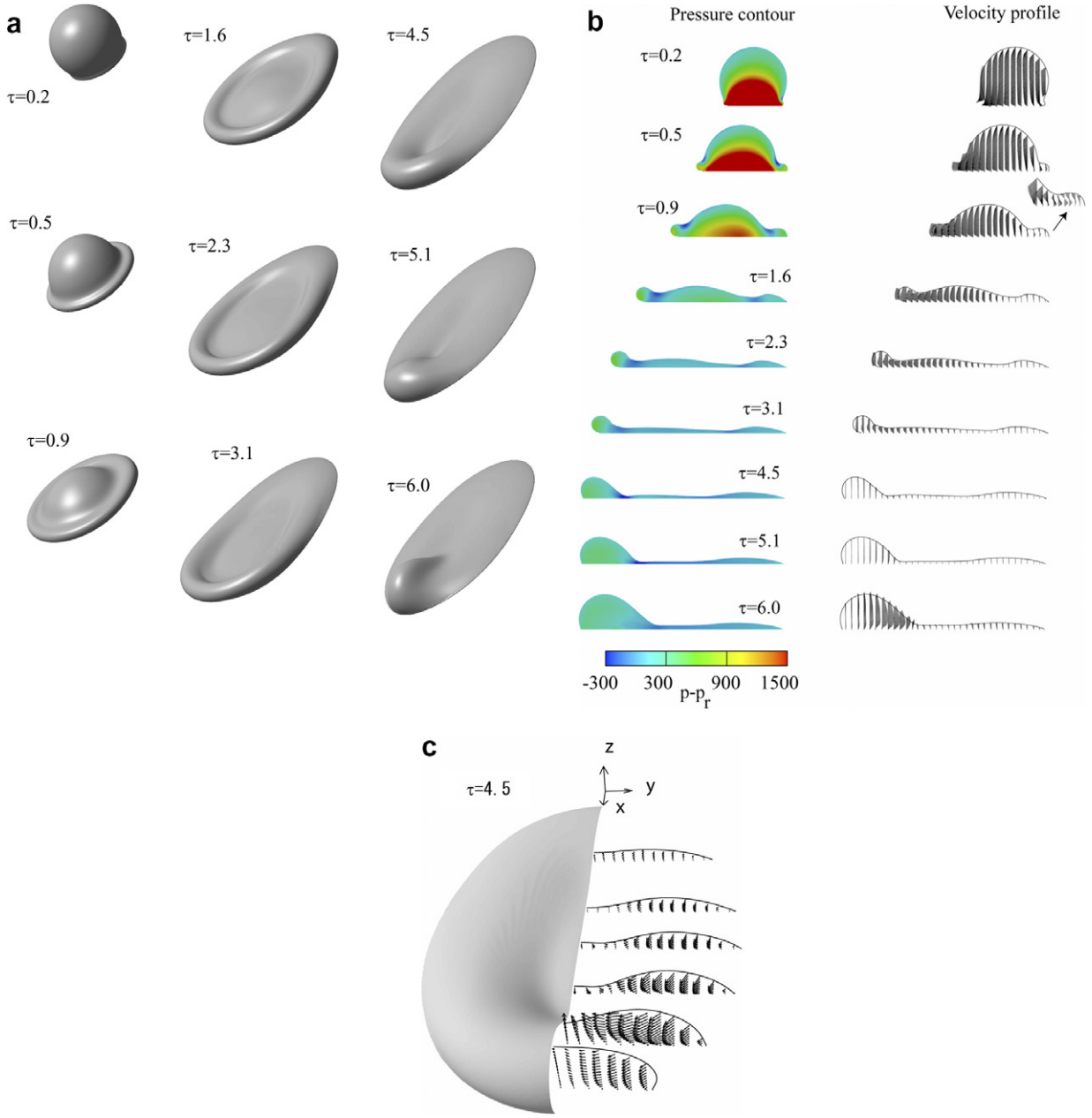

Fig. 10. Time evolution of the calculated shape of droplets (a), time evolution of the velocity profile and the pressure distribution in the liquid at symmetric plane (x–z plane) (b) and the velocity profile in the liquid (c).

due to internal shear stress and wall friction. The surface tension also reduces the liquid velocity because the pressure in the rounded edge of liquid is higher than the concave inner side. At $\tau = 4.5$, 5.1, and 6.0, it is found that the surface tension generates an upward flow of very small magnitude along the x-axis in the lower edge. At $\tau = 6.0$, liquid in the upper lower edge moves upward along the solid surface. The flow direction in the thin film is downward along the surface. The two flows encounter at the upper side of the rounded lower edge, resulting in an upward flow.

The effect of gravity is considered to be relatively small in the early stages of the oblique collision. Numerical simulations without gravity have been carried out and the results are in close agreement with those with

gravity that are shown in Figs. 8–10. The effect of gravity is thus negligible, at least in the early time stage of the process.

It should be mentioned that the protruding feature of the liquid shown in the last frame of Fig. 10a is consistent with the experiments. It has been indirectly observed by means of bottom view photographs of the droplet on a transparent glass. Fig. 11a presents a photograph showing the liquid/solid contact area during the collision in the case where the pre-impact diameter of droplet is 0.56 mm, and the impact velocity is 2.2 m/s. (The impact condition is not the same as that in Fig. 10a.) A schematic of the setup is shown in Fig. 11b. The incident angle of the light to the liquid/solid interface is 45°. Total reflection occurs at air/glass interface, while some light passes through water/glass interface, because of differing refractive index (see also Fig. 11c). The contact line can be clearly identified and the protruding part at the lower edge can be seen.

Additional simulations of oblique collisions with pre-impact diameter of droplet, d_p, of 0.53 mm and impact velocity, v_0, at 4.0 m/s have been made. The corresponding Re and We numbers are 2200 and 116, respectively. The impact inertia of droplet is approximately 35% larger than that in the previous case. The impact angle, θ, is set to 60° and 30°. Fig. 12 presents the time evolution of the predicted droplet shape. At $\tau = 0.5$, a thin circular film is formed around the bottom of the droplet with the $\theta = 60°$ case having a wider radial spread than that for the $\theta = 30°$ case. At $\tau = 1.0$, the droplet deforms into a thin circular disk for $\theta = 60°$. In the case of $\theta = 30°$, the droplet is still hemi-spherical due to the smaller velocity component normal to the solid surface. The droplet adheres to the solid in the shape of a tear-drop. Thereafter, the spreading length of the droplet in the x-direction for $\theta = 30°$ becomes noticeably longer than that for $\theta = 60°$. On the other hand, the spreading length in the y-direction (horizontal direction) is wider for the larger impact angle. As expected, asymmetry of the droplet is obvious in later time stages for smaller impact angles.

Comparisons of predicted liquid lengths along the inclined surface with the measured data are shown in Fig. 13. In both cases, the predictions agree reasonably well with the experiments. It should be noted that the dimensionless mesh size is 1/80 in x- and y-directions and $n_z = 70$ in Eq. (13) in both simulations. The number of meshes is $402 \times 122 \times 102$. In oblique collisions, the spreading length of droplet along the surface is longer for smaller impact angles, and a larger computational domain is needed to simulate the entire process. As computer resources are limited, the mesh size becomes coarser for the larger computational domain.

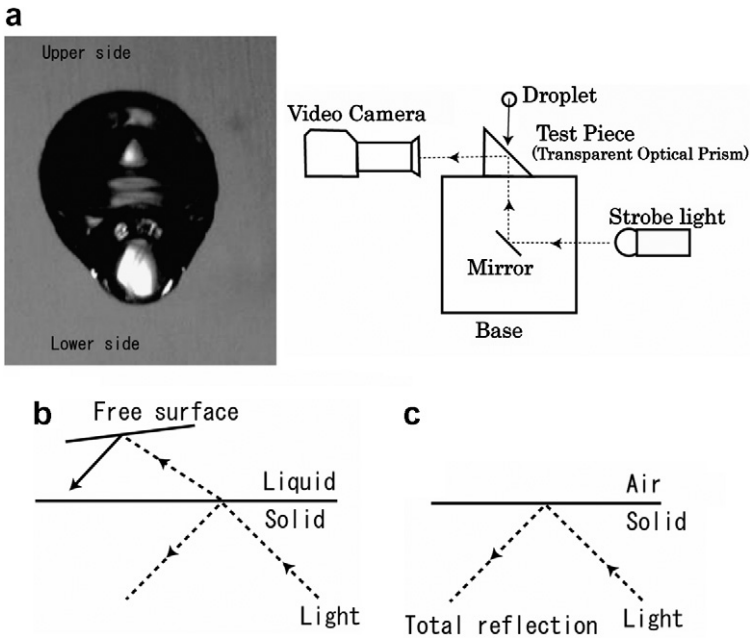

Fig. 11. A photograph showing the liquid/solid contact area for (d_p, v_0, θ) = (0.56 mm, 2.2 m/s, 45°) (a), a schematic of setup (b), and typical light paths at glass/air and glass/water interfaces (c).

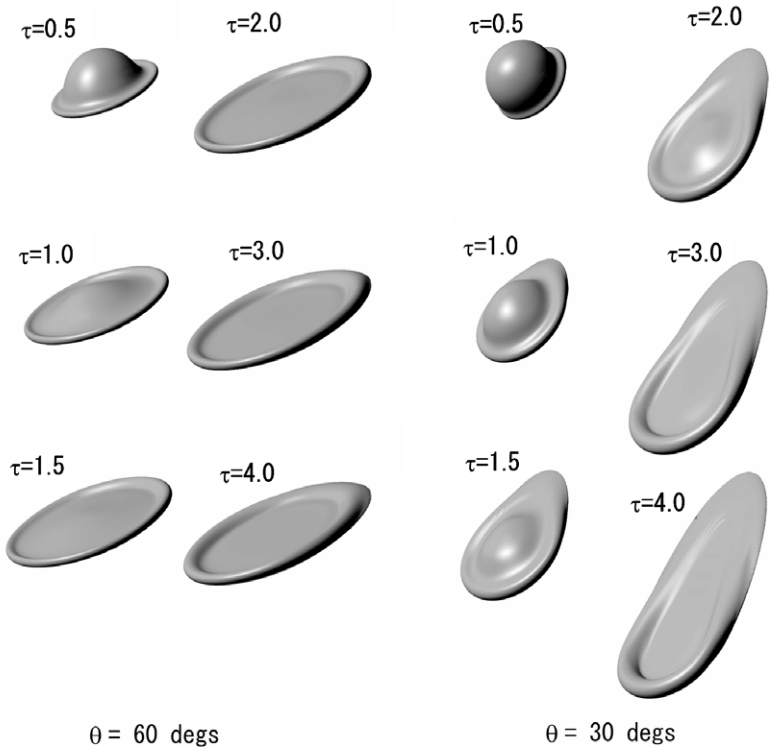

Fig. 12. Time evolution of the predicted shape of droplets for $(d_p, v_0, \theta) = (0.53\ \text{mm}, 4.0\ \text{m/s}, 60°)$ and $(d_p, v_0, \theta) = (0.53\ \text{mm}, 4.0\ \text{m/s}, 30°)$, respectively.

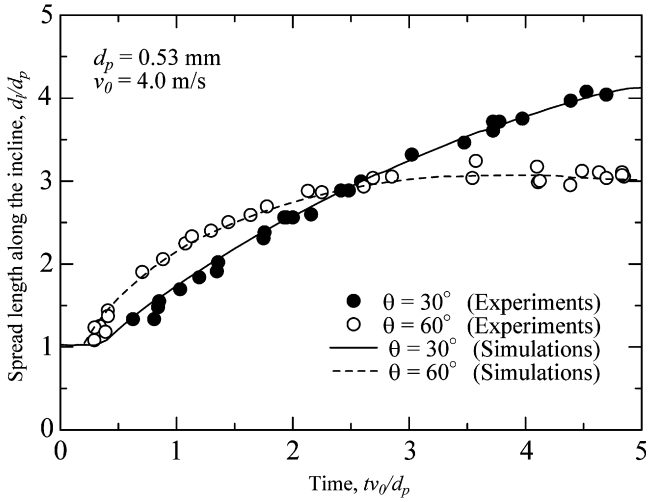

Fig. 13. Comparison of predicted liquid lengths along the inclined surface with the measured data for oblique collision.

Numerical errors caused by mesh size accumulate with time, and may become increasingly appreciable in later time stages.

It is shown in Fig. 13 that the results are in close agreement with experiments. The spread along the x-axis for $\theta = 30°$ is smaller than that for $\theta = 60°$ in the very early time stage. In both cases, the spread increases with time, with the spreading rate for the $\theta = 30°$ larger than that for the $\theta = 60°$. At approximately $\tau = 2.5$, the

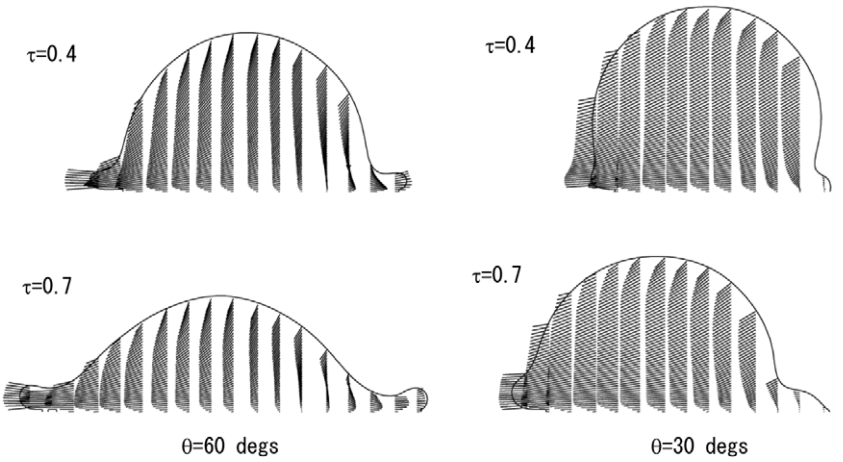

Fig. 14. Velocity profiles for $(d_p, v_0, \theta) = (0.53\ \text{mm}, 4.0\ \text{m/s}, 60°)$ and $(d_p, v_0, \theta) = (0.53\ \text{mm}, 4.0\ \text{m/s}, 30°)$, respectively.

spread length for $\theta = 30°$ surpasses that for $\theta = 60°$. Thereafter, the spread lengths for $\theta = 30°$ becomes longer. The results can be explained as follows. Immediately following the collision of a droplet with a solid, a very high pressure region appears near the impact point. The stagnation pressure at the point of impact is largest for the case of normal collision and decreases with decreasing impact angle as the component of impact inertia normal to the solid surface reduces. The high stagnation pressure causes a flow along the solid surface from the impact point, resulting in the formation of a thin liquid film. Fig. 14 presents the velocity profiles inside the droplet after the collision for $\theta = 60°$ and 30°. Magnitude of velocity vector is the same for all the figures. In the case of $\theta = 60°$, fast downward flow is seen along the solid surface in the lower edge, while relatively large upward flow arises in the upper edge. The liquid film elongates not only downward but also upward. On the other hand, the upper edge is almost stagnant for $\theta = 30°$. The spreading rate of liquid film decreases with impact angle. This explains why the diameter of droplet is larger for larger impact angle in early time stages.

In the case of oblique collisions, the droplets spread downward along the x-axis due to the component of impact inertia parallel to the solid surface. The momentum in the x-direction increases with decreasing impact angle. Thus, the droplet spread in the x-direction becomes larger for smaller impact angles except in the very early time stage.

5. Conclusions

The collision of a single droplet impinging onto a solid surface was studied by means of experiments and three-dimensional numerical simulations. The Navier–Stokes equations for incompressible viscous fluids in a three-dimensional coordinate system were solved by a finite difference method under isothermal conditions. The model was validated by comparing the predictions with experimental data. The findings of the present study are listed below.

(1) For the case of normal collisions, a droplet impinges on the surface, spreads and deforms into a thin circular disk. The predictions agree reasonably well with experiments.
(2) In the cases of oblique collision, a thin liquid film is formed around the lower bottom edge of the droplet after the impact. It spreads radially along the solid surface with time, while the height of the droplet body decreases monotonically. The shape of the liquid becomes increasingly asymmetric with time. Majority of the liquid moves downward along the surface because of impact inertia. Eventually, the lower edge of the liquid thickens and becomes rounded, while the rest of the liquid becomes very thin.
(3) The numerical results for oblique collisions are in agreement with the experimental results both qualitatively and quantitatively, at least, in the early time stage ($\tau < 5$ or so).

(4) The effect of the impact angle on the deformation behavior of droplets is as follows: in the case of normal collisions, the flow is treated as axis-symmetry. With decreasing impact angle, the shape of the droplet on the surface becomes increasingly asymmetric. The droplet spread lengthens in the x-direction, in the late time stage, and is longer for smaller impact angles.

Acknowledgements

This research was supported by Grant-in-Aid for scientific research(c) (#16560185) provided by Japan Society for the Promotion of Science and by the ISIJ research promotion grant.

References

Baer, T.A., Cairncross, R.A., Schunk, P.R., Rao, R.R., Sackinger, P.A., 2000. A finite element method for free surface flows of incompressible fluids in three dimensions. Part II, dynamic wetting lines. Int. J. Numer. Meth. Fluids 33, 405–427.

Brackbill, J.U., Kothe, D.B., Zemach, C., 1992. A continuum method for modeling surface tension. J. Comput. Phys. 100, 335–354.

Bussmann, M., Mostaghimi, J., Chandra, S., 1999. On a three-dimensional volume tracking model of drop impact. Phys. Fluids 11, 1406–1417.

Bussmann, M., Chandra, S., Mostaghimi, J., 2000. Modeling the splash of a droplet impacting a solid surface. Phys. Fluids 12, 3121–3132.

E B Dussan, V., 1979. On the spreading of liquids on solid surfaces: static and dynamic contact lines. Ann. Rev. Fluid Mech. 11, 371–400.

Francois, M., Shyy, W., 2003. Computations of drop dynamics with the immersed boundary method, part 2: drop impact and heat transfer. Numer. Heat Transfer J., Part B 44, 119–143.

Fujimoto, H., Hatta, N., 1996. Deformation and rebounding processes of a water droplet impinging on a flat surface above Leidenfrost temperature. Trans. ASME J. Fluids Eng. 118, 142–149.

Fujimoto, H., Ogino, T., Takuda, H., Hatta, N., 2001. Collision of a droplet with a hemispherical static droplet on a solid. Int. J. Multiphas. Flow 27, 1227–1245.

Fujimoto, H., Takezaki, I., Shiotani, Y., Tong, A.Y., Takuda, H., 2004. Collision dynamics of two droplets impinging successively onto a hot solid. ISIJ Int 44, 1049–1056.

Ge, Y., Fan, L.S., 2005. Three-dimensional simulation of impingement of a liquid droplet on a flat surface in the Leidenfrost regime. Phys. Fluids 17 (Art. No. 127104).

Ghafouri-Azar, R., Shakeri, S., Chandra, S., Mostaghimi, J., 2003. Interactions between molten metal droplets impinging on a solid surface. Int. J. Heat Mass Transfer 46, 1395–1407.

Ghafouri-Azar, R., Mostaghimi, J., Chandra, S., 2004. Numerical study of impact and solidification of a droplet over a deposited frozen splat. Int. J. Comput. Fluid Dyn. 18, 133–138.

Hatta, N., Fujimoto, H., Takuda, H., 1995. Deformation process of a water droplet impinging on a solid surface. Trans. ASME J. Fluids Eng. 117, 394–401.

Hirt, C.W., Nichols, B.D., 1981. Volume of fluid (VOF) method for the dynamics of free boundaries. J. Comput. Phys. 39, 201–225.

Killion, J.D., Garimella, S., 2004. Simulation of pendant droplets and falling films in horizontal tube absorbers. Trans. ASME J. Heat Transfer 126, 1003–1013.

Kothe, D.B., Mjolsness, R.C., 1992. Ripple: a new model for incompressible with free surfaces. AIAA J. 30, 2694–2700.

Pasandideh-Fard, M., Chandra, S., Mostaghimi, J., 2002. A three-dimensional model of droplet impact and solidification. Int. J. Heat Mass Transfer 45, 2229–2242.

Perot, B., Nallapati, R., 2003. A moving unstructured staggered mesh method for the simulation of incompressible free-surface flows. J. Comput. Phys. 184, 192–214.

Renardy, M., Renardy, Y., Li, J., 2001. Numerical simulation of moving contact line problems using a volume-of-fluid method. J. Comput. Phys. 171, 243–263.

Theodorakakos, A., Bergeles, G., 2004. Simulation of sharp gas–liquid interface using VOF method and adaptive grid local refinement around the interface. Int. J. Numer. Meth. Fluids 45, 421–439.

Tome, M.F., Grossi, L., Castelo, A., Cuminato, J.A., Mangiavacchi, N., Ferreira, V.G., de Sousa, F.S., McKee, S., 2004. A numerical method for solving three-dimensional generalized Newtonian free surface flows. J. Non-Newtonian Fluid Mech. 123, 85–103.

Tong, A.Y., Kasliwal, S., Fujimoto, H., Takuda, H., 2004. Numerical study on the successive impingement of droplets onto a substrate. In: Proceedings of IMECE'04, ASME International Mechanical Congress and Exposition, Anaheim, CA.

Wu, H.C., Hwang, W.S., Lin, H.J., 2004. Development of a three-dimensional simulation system for micro-inkjet and its experimental verification. Mater. Sci. Eng. A 373, 268–278.

Yabe, T., Xiao, F., Utsumi, T., 2001. The constrained interpolation profile method for multiphase analysis. J. Comput. Phys. 169, 556–593.